



Cite this: *Nanoscale*, 2021, **13**, 19133

## Coordination environment engineering on nickel single-atom catalysts for CO<sub>2</sub> electroreduction†

Mengbo Ma, Fuhua Li and Qing Tang  \*

Coordination engineering has recently emerged as a promising strategy to boost the activity of single atom catalysts (SACs) in electrocatalytic CO<sub>2</sub> reduction reactions (CO<sub>2</sub>RR). Understanding the correlation between activity/selectivity and the coordination environment would enable the rational design of more advanced SACs for CO<sub>2</sub> reduction. Herein, via density functional theory (DFT) computations, we systematically studied the effects of coordination environment regulation on the CO<sub>2</sub>RR activity of Ni SACs on C, N, or B co-doped graphene. The results reveal that the coordination environments can strongly affect the adsorption and reaction characteristics. In the C and/or N coordinated Ni–B<sub>X</sub>C<sub>Y</sub>N<sub>Z</sub> (B-free, X = 0), only Ni acts as the active site. While in the B, C and/or N coordinated Ni–B<sub>X</sub>C<sub>Y</sub>N<sub>Z</sub> (X ≠ 0), the B has transition-metal-like properties, where B and Ni function as dual-site active centers and concertedly tune the adsorption of CO<sub>2</sub>RR intermediates. The tunability in the adsorption modes and strengths also results in a weakened linear scaling relationship between \*COOH and \*CO and causes a significant activity difference. The CO<sub>2</sub>RR activity and the adsorption energy of \*COOH/\*CO are correlated to construct a volcano-type activity plot. Most of the B, C, and/or N-coordinated Ni–B<sub>X</sub>C<sub>Y</sub>N<sub>Z</sub> (X ≠ 0) are located in the left region where \*CO desorption is the most difficult step, while the C and/or N coordinated Ni–B<sub>X</sub>C<sub>Y</sub>N<sub>Z</sub> (X = 0) are located in the right region where \*COOH formation is the potential-determining step. Among all the possible Ni–B<sub>X</sub>C<sub>Y</sub>N<sub>Z</sub> candidates, Ni–B<sub>0</sub>C<sub>3</sub>N<sub>1</sub> and Ni–B<sub>1</sub>C<sub>1</sub>N<sub>2-N-oppo</sub> are predicted to be the most active and selective catalysts for the CO<sub>2</sub>RR. Our findings provide insightful guidance for developing highly effective CO<sub>2</sub>RR catalysts based on a codoped coordination environment.

Received 1st September 2021,

Accepted 19th October 2021

DOI: 10.1039/d1nr05742a

rsc.li/nanoscale

## Introduction

With the excessive consumption of non-renewable fossil fuels (coal, oil and natural gas), the increasing emission of carbon dioxide (CO<sub>2</sub>) into nature has caused severe ecological and environmental problems.<sup>1–3</sup> As an alternative way, CO<sub>2</sub> can be reduced into useful chemical products, such as carbon monoxide, methane, ethylene and methanol. However, the carbon element in CO<sub>2</sub> is in the highest +4 oxidation state and the C=O bond is highly stable, which makes it very difficult to be reduced.<sup>4–7</sup> Among the variety of developed solutions, the electrochemical reduction of CO<sub>2</sub> is one of the most promising strategies and has attracted widespread attention due to its low energy consumption, mild reaction conditions, and simple

operation, which relies on efficient catalysts to accelerate the reaction.<sup>8–10</sup> The promising electrocatalysts for the electrochemical CO<sub>2</sub> reduction reaction (CO<sub>2</sub>RR) should be able to operate at a low overpotential and can effectively control the product selectivity, inhibit the competitive hydrogen evolution reaction (HER) and maintain high electrochemical stability.<sup>11–14</sup>

Among the various types of investigated electrocatalysts,<sup>15,16</sup> single-metal-atom catalysts have developed rapidly and emerged as a promising class of catalysts for the CO<sub>2</sub>RR.<sup>17–20</sup> Compared to the metal bulk and nanoparticle counterparts, the atomically dispersed single metal catalysts have largely exposed active sites and exhibit effective atom utilization and high selectivity for the electrochemical CO<sub>2</sub>RR.<sup>21,22</sup> Moreover, their well-defined structures serve as an ideal model to establish the relationship between the structure and catalytic properties at an atomic level. To stabilize the single metal center from agglomeration, the single-metal-atom catalysts are usually coordinated and immobilized on nitrogenated carbon-based conductive substrates, such as carbon nanotubes, graphene and amorphous or porous carbon.<sup>23–25</sup> In particular, the graphene matrix has been widely used due to its high electronic conductivity and large surface area for metal loading.

School of Chemistry and Chemical Engineering, Chongqing Key Laboratory of Theoretical and Computational Chemistry, Chongqing University, Chongqing 401331, China. E-mail: qingtang@cqu.edu.cn

† Electronic supplementary information (ESI) available: Computed formation energy, dissolution potential, adsorption free energy, charge transfer, charge density difference, reaction free energy change of the elementary reaction step of CO<sub>2</sub>RR, projected density of states, and Bader charge analyses of Ni–B<sub>X</sub>C<sub>Y</sub>N<sub>Z</sub> systems. See DOI: 10.1039/d1nr05742a

Many transition metals, such as Mn, Fe, Co, Ni, and Cu,<sup>26–30</sup> have been embedded into nitrogen-doped carbon systems and investigated as CO<sub>2</sub>RR electrocatalysts. The results demonstrate that the intrinsic CO<sub>2</sub>RR activity of Fe–N–C and especially Ni–N–C catalysts to yield CO is higher than that of the Co-, Mn-, and Cu-based moieties, which even rival the state-of-the-art Au- and Ag-based catalysts.<sup>26,31–34</sup> However, the relatively strong binding of CO\* over Fe–N<sub>x</sub> and Mn–N<sub>x</sub> single sites could lead to lower selectivity for CO formation.

Particularly, apart from being cost effective, Ni single atom catalysts have displayed exceptional activity, selectivity and high stability.<sup>6,35–37</sup> Additionally, several recent experimental advances have demonstrated that the CO<sub>2</sub>RR activity of Ni–N–C entities can be effectively manipulated by controlling the local coordination environment of the Ni active center.<sup>19,38</sup> For example, Li *et al.*<sup>22</sup> realized a specific Ni–N<sub>4</sub> structure through a topo-chemical transformation strategy by carbon layer coating, which shows excellent activity and remarkable stability for the CO<sub>2</sub>RR to CO. Bao *et al.*<sup>39</sup> reported that coordinatively unsaturated Ni–N sites within porous carbon had higher selectivity and activity for the CO<sub>2</sub>RR than the Ni–N<sub>4</sub> sites. Joo *et al.*<sup>40</sup> and Lu *et al.*<sup>41</sup> both showed that the Ni–N<sub>3</sub>V (V: vacancy) sites with a shrunk Ni–N–C local structure incorporated into the graphene lattice exhibit enhanced CO<sub>2</sub>RR performance compared to the Ni–N<sub>4</sub> sites. Moreover, Jiang *et al.*<sup>42</sup> prepared a series of Ni single atom catalysts with controlled Ni–N coordination numbers (Ni–N<sub>x</sub>–C,  $x = 2, 3, 4$ ) by varying the pyrolysis temperature of the polypyrrole@MgNi-MOF-74 precursor. They revealed that the Ni–N<sub>2</sub>–C catalyst with Ni coordinated by two N and two C shows far superior CO faradaic efficiency and turnover frequency compared to the Ni–N<sub>3</sub>–C and Ni–N<sub>4</sub>–C counterparts. Cheng *et al.*<sup>43</sup> fabricated Ni-based catalysts with various N/C coordination numbers (Ni@N<sub>x</sub>C<sub>y</sub>) through pyrolysis of carbon substrates at different temperatures and achieved an optimal catalytic performance for the

Ni@N<sub>2</sub>C<sub>2</sub> catalysts. Theoretically, Zhang *et al.*<sup>11</sup> suggested that the graphene embedded Ni–N<sub>5</sub> site with additional ligated axial N atoms exhibits lower CO<sub>2</sub>RR onset overpotential than the Ni–N<sub>4</sub> site.

This recent progress has evidenced the strong potential of coordination environment regulation in tuning the CO<sub>2</sub>RR activity of a single metal center. In principle, due to the difference in electronegativity and atomic size, changing the surrounding coordination elements will modify the electronic structure of the metal center, which would essentially affect the adsorption strength of the reaction intermediates and in turn, modify the activity and selectivity. It is noteworthy that, in addition to the widely studied Ni–N<sub>x</sub>C<sub>y</sub> catalysts with Ni–N and Ni–C coordination environments, many recent studies have shown that boron can be doped into the carbon matrix and the incorporation of boron can greatly accelerate the electrocatalytic reactions.<sup>44–46</sup> The boron (~0.82 Å) has a comparable covalent radius with C (~0.77 Å) and N (~0.75 Å), which can form rich compounds with C (e.g., BC<sub>3</sub>),<sup>47</sup> N (BN)<sup>48,49</sup> and Ni (e.g., NiB, Ni<sub>2</sub>B, Ni<sub>3</sub>B, Ni<sub>4</sub>B<sub>3</sub>).<sup>50</sup> Moreover, B, in many cases, functions like a transition metal since the hybridization of its non-fully occupied valence electrons supplies a great chance to accept and donate lone-pair electrons. Hence, B can also be a potential element to dope and adjust the coordination environment.

In this research, we investigate the CO<sub>2</sub>RR performance of Ni-centered graphene with various B/C/N coordination environments from density functional theory (DFT) calculations. Recently, Goddard and Luo *et al.*<sup>51</sup> reported a comprehensive study of the CO<sub>2</sub>RR mechanism on C/N coordinated Ni SAC by taking kinetics, the solvation effect, and experiment comparison into consideration. The CO<sub>2</sub>RR performance varies remarkably by differences in the number of C or N bonded to Ni. Herein, we used the computational hydrogen electrode model with a number of simplifications and approximations for fast screening the potential catalysts by calculating the thermodynamic energetics. This simplified model, in most cases, allows the reliable alignment of theoretical electrochemical potentials to those measured in experiment. Compared to the prior theoretical studies that mainly focus on the N and C coordination,<sup>51,52</sup> the hybrid coordination by non-metal C, N and transition-metal-like B leads to more versatile adsorption characteristics and diverse activities. Our results showed that most of the Ni–B<sub>X</sub>C<sub>Y</sub>N<sub>Z</sub> ( $X + Y + Z = 4$ ) catalysts (25 out of 27 possible candidates) have high thermodynamic and electrochemical stability. The adsorption modes of CO<sub>2</sub>, \*COOH and \*CO are versatile. In the case of C and/or N coordinated Ni–B<sub>X</sub>C<sub>Y</sub>N<sub>Z</sub> (B-free,  $X = 0$ ), only the Ni center acts as the active site, and the CO<sub>2</sub> hydrogenation to \*COOH is the potential-determining step. While in the case of B-coordinated Ni–B<sub>X</sub>C<sub>Y</sub>N<sub>Z</sub> ( $X \neq 0$ ), the B can actively participate in the reaction. As a result, the Ni and B function as dual sites to flexibly tune the adsorption of CO<sub>2</sub>RR intermediates, which facilitate the CO<sub>2</sub> hydrogenation but increase the adsorption strength of \*CO, making \*CO desorption the most difficult step. Because of the versatile single- and dual-site adsorption modes, the



Qing Tang

*Qing Tang is a Professor of Chemistry at Chongqing University. She received her B.S. in Chemistry from Shenzhen University in 2009, and her Ph.D. in Chemistry from Nankai University in 2014. After three years of postdoctoral research at the University of California Riverside (UCR), she joined the faculty at the school of chemistry and chemical engineering at Chongqing University in 2018. Her current research interests*

*focus on the application of multi-scale computational methods to understand, design and discover new materials for electrocatalytic applications, such as hydrogen evolution, oxygen reduction and CO<sub>2</sub> conversion.*

scaling relationship between the adsorption energy of  $^*\text{COOH}$  and  $^*\text{CO}$  is significantly weakened. Moreover, we build the correlation between the adsorption energy and the limiting potential to describe the activity and selectivity. Compared to the pure N-coordinated Ni, the hybrid coordination by C–N, B–N or B–C–N can lead to much higher electrocatalytic activity, and several highly promising candidates stand out with high  $\text{CO}_2\text{RR}$  activity and selectivity, including  $\text{Ni-B}_0\text{C}_3\text{N}_1$ ,  $\text{Ni-B}_1\text{C}_0\text{N}_3$ ,  $\text{Ni-B}_2\text{C}_0\text{N}_{2-\text{B-hex}}$ ,  $\text{Ni-B}_1\text{C}_1\text{N}_{2-\text{N-oppo}}$ , and  $\text{Ni-B}_1\text{C}_1\text{N}_{2-\text{N-hex}}$ . These results provide useful insights into the understanding of the coordination effect on the  $\text{CO}_2\text{RR}$  and offer a reference for further research on advanced electrocatalysts.

## Computational details

All the spin-unrestricted DFT computations are carried out in the DMol<sup>3</sup> code.<sup>53</sup> The generalized gradient approximation (GGA)<sup>54</sup> of the Perdew–Burke–Ernzerhof (PBE)<sup>55</sup> functional is used to describe the exchange–correlation interactions and the core electrons are treated with semi-core pseudopotentials (DSPPs).<sup>56</sup> The double numerical plus polarization (DNP) basis is adopted and the global orbital cut off value is set as 4.0 Å. The convergence tolerance of geometry optimization is set as  $2.0 \times 10^{-5}$  Ha in energy, 0.004 Ha Å<sup>-1</sup> in force, and the force exerted on each atom is set to be 0.005 Å. To simulate the aqueous solvent environment, a conductor-like screening model (COSMO) with a dielectric constant of 78.54 is used.<sup>57</sup> The  $k$ -points mesh of  $5 \times 5 \times 1$  and  $9 \times 9 \times 1$  using the Monkhorst–Pack method<sup>58</sup> is utilized for the structural optimization and electronic property calculations, respectively.

The absorption free energy of  $\text{CO}_2$  on  $\text{Ni-B}_x\text{C}_y\text{N}_z$  is calculated by:  $\Delta G_{\text{ads}} = \Delta E_{\text{ads}} + \Delta ZPE - T\Delta S$ , where  $\Delta E_{\text{ads}}$  is the adsorption energy obtained by subtracting the total energy of the isolated  $\text{Ni-B}_x\text{C}_y\text{N}_z$  catalyst and free  $\text{CO}_2$  molecule from the adsorbed system. Due to the inaccurate description of  $\text{CO}_2$  molecule by the PBE functional, we added a correction of +0.10 eV for  $\text{CO}_2$ .<sup>59</sup>

The change of Gibbs free energy ( $\Delta G$ ) for each elementary reaction step is calculated using the equation:  $\Delta G = \Delta E + \Delta ZPE - T\Delta S + \Delta G_{\text{U}}$ , where  $\Delta E$  is the electronic reaction energy of a certain reaction step directly obtained from DFT energies,  $\Delta G_{\text{U}} = -eU$ , with  $U$  being the electrode potential of the electrochemical step.  $\Delta ZPE$  and  $T\Delta S$  are the contributions of the zero-point energy and entropy, respectively, which originate from the calculation of vibrational frequencies of the adsorbed intermediates at  $T = 298.15$  K. The entropy of gas phase molecules is derived from the NIST database. The detailed data are provided in the ESI.†

## Results and discussion

### Catalyst models and stability

As shown in Fig. 1, we use a  $6 \times 6 \times 1$  graphene supercell with two C vacancies as the original substrate to construct the

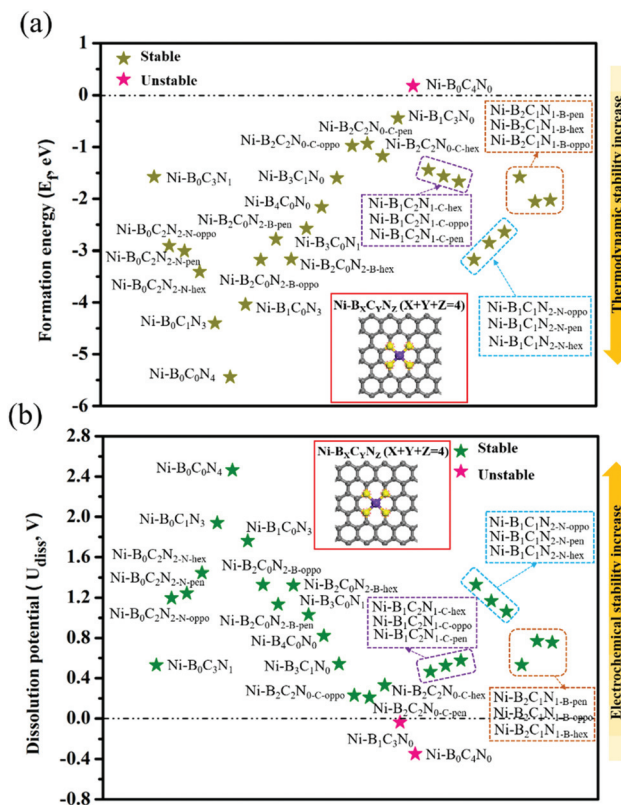
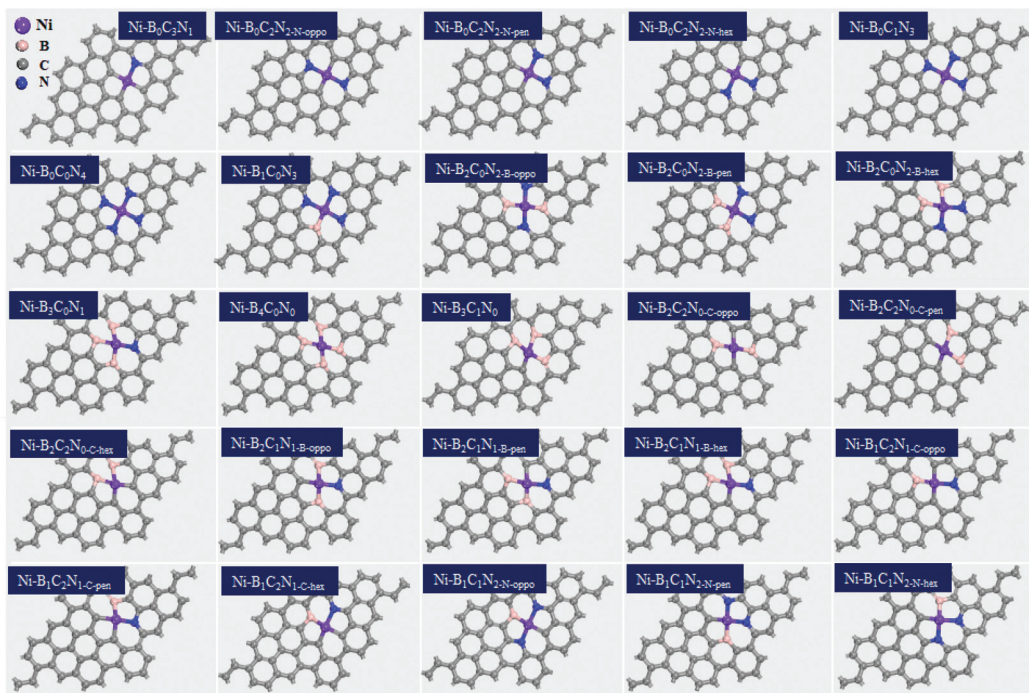


Fig. 1 The DFT-computed formation energy (a) and dissolution potential (b) of  $\text{Ni-B}_x\text{C}_y\text{N}_z$  ( $X + Y + Z = 4$ ). The inset shows the top view of the catalyst model, where the highlighted yellow atoms represent the coordination atoms of the Ni center (purple atom).

model catalysts, and then a single Ni atom is placed into the vacancy center and binds to four pyridine-like coordination atoms (B, C or N). The corresponding catalyst models are named  $\text{Ni-B}_x\text{C}_y\text{N}_z$  ( $X + Y + Z = 4$ ). Note that there are three possible coordination configurations when  $X$ ,  $Y$  or  $Z = 2$ , denoted as  $\text{Ni-B}_x\text{C}_y\text{N}_z\text{-oppo}$ ,  $\text{Ni-B}_x\text{C}_y\text{N}_z\text{-pen}$ , and  $\text{Ni-B}_x\text{C}_y\text{N}_z\text{-hex}$ , in which the same two atoms occupy the opposite coordination sites or neighboring coordination sites in penta-atomic and hex-atomic rings, respectively. Ultimately, 27 catalyst structures are constructed.

In order to characterize the thermodynamic stability, we calculated the formation energy ( $E_f$ ) of  $\text{Ni-B}_x\text{C}_y\text{N}_z$  systems, defined as  $E_f = E_{\text{total}} - n_B\mu_B - n_C\mu_C - n_N\mu_N - E_{\text{Ni}}$ . Here,  $E_{\text{total}}$  is the total energy of  $\text{Ni-B}_x\text{C}_y\text{N}_z$ .  $\mu_B$ ,  $\mu_C$  and  $\mu_N$  represent the chemical potential of B, C, and N, which corresponds to the energy of a single carbon atom in graphene, a single boron atom in planar hexagonal  $\text{B}_{36}$ ,<sup>60</sup> and half of the energy of  $\text{N}_2$  molecules, respectively. While  $n_B$ ,  $n_C$ , and  $n_N$  stand for the number of corresponding coordination atoms in  $\text{Ni-B}_x\text{C}_y\text{N}_z$ ,  $E_{\text{Ni}}$  is the energy of the isolated Ni atom. From Fig. 1a, one can see that except for the pure carbon coordinated  $\text{Ni-B}_0\text{C}_4\text{N}_0$ , the calculated  $E_f$  values of the other 26  $\text{Ni-B}_x\text{C}_y\text{N}_z$  catalysts are all negative (−0.94 to −5.44 eV), indicating their high thermodynamic stabilities and high synthetic potential in experiments. In addition, the dissolution potential  $U_{\text{diss}}$  is another



**Fig. 2** The optimized structures (top view) of the screened 25  $\text{Ni-B}_X\text{C}_Y\text{N}_Z$  ( $X + Y + Z = 4$ ), the color modes: purple for Ni, pink for B, blue for N, and grey for C.

important parameter to evaluate the electrochemical stabilities in a realistic electrochemical environment.<sup>61,62</sup> The  $U_{\text{diss}}$  is calculated as  $U_{\text{diss}} = U_{\text{diss(metal)}}^{\circ} - E_f/ne$ , where  $U_{\text{diss(metal)}}^{\circ}$  is the standard dissolution potential of the Ni metal,  $E_f$  is the formation energy, and  $n$  is the number of electrons involved in the dissolution (herein  $n = 2$ ). According to this definition, only a catalyst with  $U_{\text{diss}} > 0$  V vs. SHE can stably exist under acidic electrochemical conditions (the exact values of  $E_f$  and  $U_{\text{diss}}$  are listed in Table S1†).<sup>61,62</sup> Among the 27  $\text{Ni-B}_X\text{C}_Y\text{N}_Z$  systems, only  $\text{Ni-B}_1\text{C}_3\text{N}_0$  and  $\text{Ni-B}_0\text{C}_4\text{N}_0$  are excluded due to their negative  $U_{\text{diss}}$  and electrochemical instability (Fig. 1b). Finally, after the stability screening, there are about 25  $\text{Ni-B}_X\text{C}_Y\text{N}_Z$  structures that both meet the criteria of thermodynamic and electrochemical stability. The corresponding structures of the 25  $\text{Ni-B}_X\text{C}_Y\text{N}_Z$  are displayed in Fig. 2, which are further investigated as the candidate catalysts of the  $\text{CO}_2\text{RR}$ .

### Adsorption of reaction species

The activation of  $\text{CO}_2$  as well as the adsorption of reaction intermediates (e.g.,  $^*\text{COOH}$ ,  $^*\text{CO}$ ) onto the surface of catalysts plays a critical role during the electrocatalytic  $\text{CO}_2\text{RR}$ . Hence, we firstly investigated the adsorption behaviors, and the most stable adsorption configurations for  $^*\text{CO}_2$ ,  $^*\text{COOH}$  and  $^*\text{CO}$  are shown in Fig. 3 (the detailed adsorption free energy and charge transfer values are listed in Table S2†). From Fig. 3a, the  $^*\text{CO}_2$  adsorption has two types of adsorption modes: physical adsorption and chemical adsorption. Among them, about 22  $\text{Ni-B}_X\text{C}_Y\text{N}_Z$  compositions form physisorption. On  $\text{Ni-B}_X\text{C}_Y\text{N}_Z$  ( $X = 0$ ),  $\text{Ni-B}_X\text{C}_Y\text{N}_Z$  ( $X = 1, 2$ (pen);  $Y = 0$ ),  $\text{Ni-B}_X\text{C}_Y\text{N}_Z$  ( $X = 1; Y = 2; Z = 1$ ) and  $\text{Ni-B}_X\text{C}_Y\text{N}_Z$  ( $X = 1; Y = 1; Z = 2$ (hex)), the

$\text{CO}_2$  is physically adsorbed with the C atom of  $\text{CO}_2$  pointed above the Ni center. While for  $\text{Ni-B}_X\text{C}_Y\text{N}_Z$  ( $X = 2$ (oppo, hex), 3, 4;  $Y = 0$ ),  $\text{Ni-B}_X\text{C}_Y\text{N}_Z$  ( $Y = 1, 2; Z = 0$ ) and  $\text{Ni-B}_X\text{C}_Y\text{N}_Z$  ( $X = 2$ (oppo, hex);  $Y = 1; Z = 1$ ), the  $\text{CO}_2$  is physically adsorbed with the O atom of  $\text{CO}_2$  pointed above the Ni center. In the case of physical adsorption, the calculated  $\text{CO}_2$  adsorption free energy is around  $-0.09\text{--}0.20$  eV, and the charge transfer between  $\text{CO}_2$  and  $\text{Ni-B}_X\text{C}_Y\text{N}_Z$  is around  $0.004\text{--}0.019|e|$  from Bader charge analysis. In the case of chemical adsorption, there also exist two types of binding modes. On  $\text{Ni-B}_2\text{C}_1\text{N}_1\text{-B-pen}$ ,  $\text{CO}_2$  is chemically adhered with both the C and O atoms bonded to the Ni atom, leading to a favorable adsorption free energy of  $-0.18$  eV, substantial charge transfer of  $0.36|e|$ , and curved O-C-O bond angle of  $145.8^\circ$ . Differently, on  $\text{Ni-B}_1\text{C}_1\text{N}_2\text{-N-oppo}$  and  $\text{Ni-B}_1\text{C}_1\text{N}_2\text{-N-pen}$ , the C atom of chemisorbed  $\text{CO}_2$  is bonded to the Ni atom, while the O atom is bonded to the coordinated B atom. The dual-site activation of  $\text{CO}_2$  results in stronger adsorption energies ( $-0.25$  and  $-0.39$  eV), larger charge transfer ( $0.76$  and  $0.96|e|$ ), and stronger deviation of the O-C-O bond angle from linearity ( $130.8^\circ$  and  $129.3^\circ$ ). The charge density difference of  $\text{Ni-B}_2\text{C}_1\text{N}_1\text{-B-pen}$ ,  $\text{Ni-B}_1\text{C}_1\text{N}_2\text{-N-oppo}$  and  $\text{Ni-B}_1\text{C}_1\text{N}_2\text{-N-pen}$  with chemically captured  $\text{CO}_2$  is shown in Fig. S1.† One can see that the Ni center and the directly coordinated N, C or B atom are the main player in the activation and orbital interaction with the  $\text{CO}_2$  reactant.

From Fig. 3b, the  $^*\text{COOH}$  has versatile adsorption modes, which can be divided into five types. Specifically, (i) on  $\text{Ni-B}_X\text{C}_Y\text{N}_Z$  ( $X = 0$ ),  $\text{Ni-B}_X\text{C}_Y\text{N}_Z$  ( $X = 2$ (hex), 3;  $Y = 0$ ) and  $\text{Ni-B}_X\text{C}_Y\text{N}_Z$  ( $X = 2$ (hex);  $Z = 0$ ), the C atom of  $^*\text{COOH}$  is singly bonded to the Ni active center; (ii) on  $\text{Ni-B}_4\text{C}_0\text{N}_0$ ,  $\text{Ni-B}_3\text{C}_1\text{N}_0$ ,  $\text{Ni}$

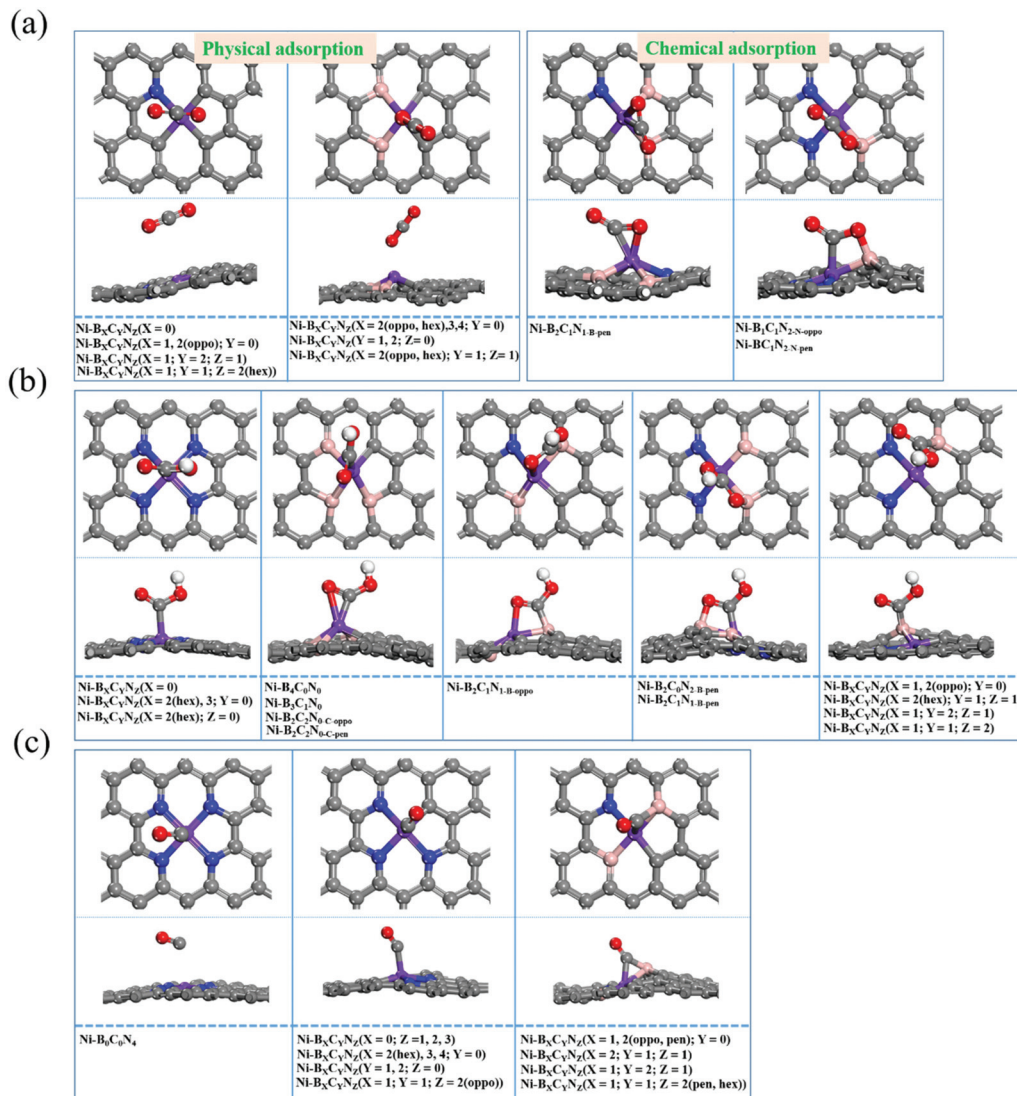


Fig. 3 The different adsorption modes of \*CO<sub>2</sub> (a), \*COOH (b), and \*CO (c) intermediates on Ni-B<sub>X</sub>C<sub>Y</sub>N<sub>Z</sub>.

B<sub>2</sub>C<sub>2</sub>N<sub>0</sub>-C-oppo and Ni-B<sub>2</sub>C<sub>2</sub>N<sub>0</sub>-C-pen, both the C and O atoms of \*COOH are co-adsorbed onto the Ni atom; (iii) on Ni-B<sub>2</sub>C<sub>1</sub>N<sub>1</sub>-B-oppo, the C atom of \*COOH is bonded to a B atom while the O atom is bonded to the Ni atom; (iv) conversely, on Ni-B<sub>2</sub>C<sub>0</sub>N<sub>2</sub>-B-pen and Ni-B<sub>2</sub>C<sub>1</sub>N<sub>1</sub>-B-pen, the C of \*COOH is bonded with Ni while the O atom binds with the B atom; (v) on Ni-B<sub>X</sub>C<sub>Y</sub>N<sub>Z</sub> (X = 1, 2(oppo); Y = 0), Ni-B<sub>X</sub>C<sub>Y</sub>N<sub>Z</sub> (X = 2(hex); Y = 1; Z = 1), Ni-B<sub>X</sub>C<sub>Y</sub>N<sub>Z</sub> (X = 1; Y = 2; Z = 1) and Ni-B<sub>X</sub>C<sub>Y</sub>N<sub>Z</sub> (X = 1; Y = 1; Z = 2), the C atom of \*COOH is singly bonded to the B atom, which indicates that the B acts as the active center. Moreover, from Fig. 3c, the \*CO can have three types of adsorption modes. (i) On Ni-B<sub>0</sub>C<sub>0</sub>N<sub>4</sub>, the \*CO is physically adsorbed on the catalyst; (ii) on Ni-B<sub>X</sub>C<sub>Y</sub>N<sub>Z</sub> (X = 0; Z = 1, 2, 3), Ni-B<sub>X</sub>C<sub>Y</sub>N<sub>Z</sub> (X = 2(hex), 3, 4; Y = 0), Ni-B<sub>X</sub>C<sub>Y</sub>N<sub>Z</sub> (Y = 1, 2; Z = 0) and Ni-B<sub>X</sub>C<sub>Y</sub>N<sub>Z</sub> (X = 1; Y = 1; Z = 2(oppo)), the \*CO is chemically adsorbed at the Ni center forming Ni-C single bonds; (iii) on Ni-B<sub>X</sub>C<sub>Y</sub>N<sub>Z</sub> (X = 1, 2(oppo, pen); Y = 0), Ni-B<sub>X</sub>C<sub>Y</sub>N<sub>Z</sub> (X = 2; Y = 1; Z = 1), Ni-B<sub>X</sub>C<sub>Y</sub>N<sub>Z</sub> (X = 1; Y = 2; Z = 1) and Ni-B<sub>X</sub>C<sub>Y</sub>N<sub>Z</sub> (X = 1; Y = 1; Z = 2(hex))

= 1; Z = 2(pen, hex)), the \*CO forms bridging coordination with the Ni and B atoms. These flexible and versatile adsorption modes of CO<sub>2</sub>, \*COOH and \*CO indicate that not only the Ni center but also the non-metal coordination atoms, B, in particular, play a vital role in tuning and stabilizing the reaction intermediates.

#### Scaling relations

The reduction of CO<sub>2</sub> to CO is a two-electron reaction, which includes two step hydrogenations of carbonaceous intermediates, *i.e.*, \*CO<sub>2</sub> + H<sup>+</sup> + e<sup>-</sup> → \*COOH and \*COOH + H<sup>+</sup> + e<sup>-</sup> → \*CO + H<sub>2</sub>O. On the traditional metal surfaces, the adsorption energies of \*COOH and \*CO are usually linearly correlated,<sup>63</sup> and the weak \*COOH or \*CO adsorption (\*COOH formation becomes unfavorable) can lead to a low CO<sub>2</sub>RR activity, while a strong \*COOH or \*CO adsorption makes the release of the CO product become difficult. Therefore, how to break or weaken the linear scaling relationship between \*COOH and \*CO has

long been pursued in the CO<sub>2</sub>RR study. In our case, we also examined the correlation between \*COOH and \*CO. The adsorption energy ( $E_{\text{ads}}$ ) of \*COOH and \*CO on Ni-B<sub>X</sub>C<sub>Y</sub>N<sub>Z</sub> is calculated using the equation:

$$E_{\text{ads}}(*\text{COOH}) = E_{(\text{Ni-B}_X\text{C}_Y\text{N}_Z + \text{COOH})} - E_{(\text{Ni-B}_X\text{C}_Y\text{N}_Z)} - E_{\text{CO}_2(\text{g})} - 1/2E_{\text{H}_2} \quad (1)$$

$$E_{\text{ads}}(*\text{CO}) = E_{(\text{Ni-B}_X\text{C}_Y\text{N}_Z + \text{CO})} - E_{(\text{Ni-B}_X\text{C}_Y\text{N}_Z)} - E_{\text{CO}(\text{g})} \quad (2)$$

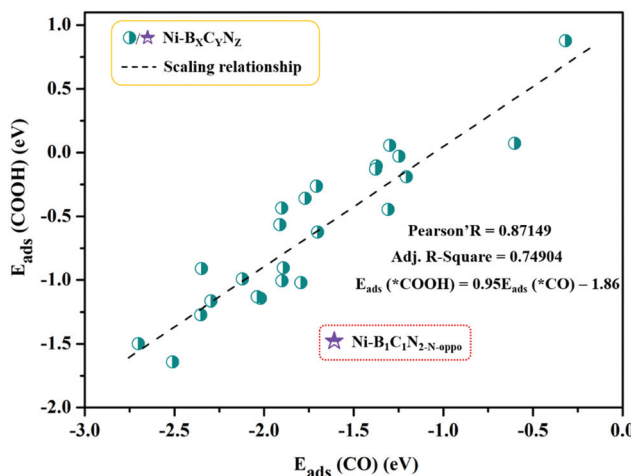


Fig. 4 Scaling relationship between the adsorption energies of \*COOH ( $E_{\text{ads}}(*\text{COOH})$ ) and \*CO ( $E_{\text{ads}}(*\text{CO})$ ).

The calculated adsorption energies are provided in Table S3,† and the correlation between  $E_{\text{ads}}$  (\*COOH) and  $E_{\text{ads}}$  (\*CO) is shown in Fig. 4. From Fig. 4, the adsorption energy of \*COOH and \*CO follows a fitted linear relationship  $E_{\text{ads}}(*\text{COOH}) = 0.95E_{\text{ads}}(*\text{CO}) - 1.86$ , and the scaling relations ( $R \approx 0.87$ ) between them are slightly weakened with scattered points compared to those of pure metal surfaces ( $R \approx 0.96$ ).<sup>63</sup> A special case is Ni-B<sub>1</sub>C<sub>1</sub>N<sub>2-N-oppo</sub>, which deviates greatly from the overall linear correlation. Note that on the pure metal surfaces, the \*COOH and \*CO are uniformly adsorbed to the surface metal atoms *via* single coordination mode (C-M bond). However, in our Ni-B<sub>X</sub>C<sub>Y</sub>N<sub>Z</sub> systems, the change of coordination environment, especially with the introduction of B, leads to versatile coordination modes (e.g., single or dual-site coordination) that vary greatly with the type and number of coordination elements. The versatility in the adsorption structures could be the main reason for the weakened linear scaling between \*COOH and \*CO in Ni-B<sub>X</sub>C<sub>Y</sub>N<sub>Z</sub>.

### CO<sub>2</sub>RR activity and selectivity

As discussed above, the adsorption characteristics of CO<sub>2</sub>, \*COOH and CO varied with the change of coordination environments, which indicates that the activity and product selectivity would be significantly affected. Thus, we further explored the activity of the CO<sub>2</sub>RR to CO. The CO<sub>2</sub>RR pathways can be divided into four elementary steps (Fig. 5a): (i) CO<sub>2</sub> adsorption: CO<sub>2</sub> (g) + \* → \*CO<sub>2</sub>; (ii) \*COOH formation: \*CO<sub>2</sub> + H<sup>+</sup> + e<sup>-</sup> → \*COOH; (iii) \*CO formation: \*COOH + H<sup>+</sup> + e<sup>-</sup> →

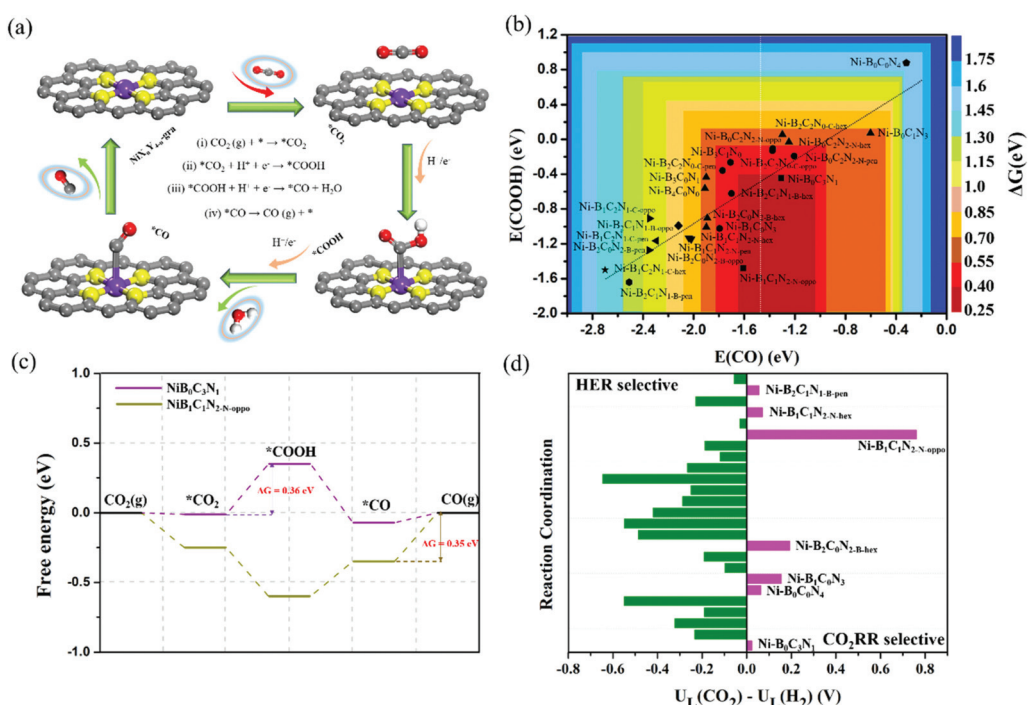


Fig. 5 Schematic of the four-step reaction processes of CO<sub>2</sub> reduction to CO on Ni-B<sub>X</sub>C<sub>Y</sub>N<sub>Z</sub> (a). 2D volcano plot for CO evolution on Ni-B<sub>X</sub>C<sub>Y</sub>N<sub>Z</sub> catalysts (b). Free energy diagrams for the CO<sub>2</sub>RR on Ni-B<sub>0</sub>C<sub>3</sub>N<sub>1</sub> and Ni-B<sub>1</sub>C<sub>1</sub>N<sub>2-N-oppo</sub> (c). The limiting potential difference between CO<sub>2</sub> reduction ( $U_L(\text{CO}_2)$ ) and HER ( $U_L(\text{H}_2)$ ) on various Ni-B<sub>X</sub>C<sub>Y</sub>N<sub>Z</sub> catalysts (d).

\*CO + H<sub>2</sub>O; and (iv) \*CO desorption: \*CO → CO (g) + \*. The Gibbs free energy changes ( $\Delta G$ ) for each reaction step are provided in Tables S4–S6,† and the  $\Delta G$  ( $\Delta G = \max(\Delta G_{\text{i}}, \Delta G_{\text{ii}}, \Delta G_{\text{iii}}, \Delta G_{\text{iv}})$ ) of the most difficult step, or the most sluggish step, dictates the reaction activity. The activity as a function of the binding energy of COOH and CO is shown in Fig. 5b. It is worth noting that the activity diagram is divided into two regions. In the right region, the \*CO adsorption is relatively weak, and the activity is determined by the potential-dependent protonation of \*CO<sub>2</sub> to \*COOH (step ii); while in the left region, the \*CO adsorption is strong, and the activity is determined by the thermodynamic-dependent \*CO desorption (\*CO → \* + CO<sub>(g)</sub>, step iv). Clearly, most of the B-coordinated B<sub>X</sub>C<sub>Y</sub>N<sub>Z</sub> ( $X \neq 0$ ) catalysts are located in the left region, where  $\Delta G$  (\*CO) varies from −0.35 to −1.42 eV, and the \*CO desorption becomes the most difficult step. While Ni–B<sub>2</sub>C<sub>2</sub>N<sub>0-C-oppo</sub>, Ni–B<sub>2</sub>C<sub>2</sub>N<sub>0-C-hex</sub>, and all the C and/or N coordinated Ni–B<sub>X</sub>C<sub>Y</sub>N<sub>Z</sub> ( $X = 0$ ) systems are located in the right region, where the \*COOH formation becomes the potential-determining step, and the corresponding free energy change of \*CO<sub>2</sub> hydrogenation to \*COOH varies from 0.36 to 1.49 eV. Note that for the B-free Ni–B<sub>X</sub>C<sub>Y</sub>N<sub>Z</sub> ( $X = 0$ ), the CO<sub>2</sub>RR activity is gradually decreased as the number of coordinated nitrogen atoms increases (Ni–B<sub>0</sub>C<sub>3</sub>N<sub>1</sub> > Ni–B<sub>0</sub>C<sub>2</sub>N<sub>2-N-oppo</sub> ≈ Ni–B<sub>0</sub>C<sub>2</sub>N<sub>2-N-pen</sub> > Ni–B<sub>0</sub>C<sub>2</sub>N<sub>2-N-hex</sub> ≈ Ni–B<sub>0</sub>C<sub>1</sub>N<sub>3</sub> > Ni–B<sub>0</sub>C<sub>0</sub>N<sub>4</sub>). Moreover, from the volcano plot, Ni–B<sub>0</sub>C<sub>3</sub>N<sub>1</sub> (the bottom of the right region) and Ni–B<sub>1</sub>C<sub>1</sub>N<sub>2-N-oppo</sub> (the bottom of the left region) stand out as the most active catalysts for the CO<sub>2</sub>RR. Along the right region, the Ni–B<sub>0</sub>C<sub>3</sub>N<sub>1</sub> has the lowest free energy (0.36 eV) for the reaction-limiting step (\*CO<sub>2</sub> + H<sup>+</sup> + e<sup>−</sup> → \*COOH); and along the left region, the Ni–B<sub>1</sub>C<sub>1</sub>N<sub>2-N-oppo</sub> has the lowest desorption energy for \*CO release (−0.35 eV). The detailed free energy diagram of CO<sub>2</sub> reduction on Ni–B<sub>0</sub>C<sub>3</sub>N<sub>1</sub> and Ni–B<sub>1</sub>C<sub>1</sub>N<sub>2-N-oppo</sub> is shown in Fig. 5c.

Furthermore, to compare the computational accuracy of DMol<sup>3</sup> with the plane-wave basis method in the VASP code, we choose the six N/C coordinated Ni–B<sub>X</sub>C<sub>Y</sub>N<sub>Z</sub> ( $X = 0$ ) systems to calculate the free energy diagram for CO evolution (Fig. S2†), and the free energy change for the potential-determining step (\*COOH formation) is summarized in Table S7.† The free energy change predicted by the two methods differs by about 0.06–0.2 eV, and the trend of the predicted activity is similar except for Ni–B<sub>0</sub>C<sub>2</sub>N<sub>2</sub> and Ni–B<sub>0</sub>C<sub>1</sub>N<sub>3</sub> (DMol<sup>3</sup> predicts a higher activity of Ni–B<sub>0</sub>C<sub>2</sub>N<sub>2-N-oppo</sub>/Ni–B<sub>0</sub>C<sub>2</sub>N<sub>2-N-pen</sub> over Ni–B<sub>0</sub>C<sub>1</sub>N<sub>3</sub>, while VASP predicts the opposite). Recent studies by Luo *et al.*<sup>51</sup> applied a grand canonical potential kinetics method to predict the reaction mechanism and rates for the CO<sub>2</sub>RR over Ni–N<sub>2</sub>C<sub>2</sub>, Ni–N<sub>3</sub>C<sub>1</sub>, and Ni–N<sub>4</sub> sites in graphene. They revealed that Ni–N<sub>2</sub>C<sub>2</sub> leads to the lowest onset potential (−0.84 V to achieve 10 mA cm<sup>−2</sup> current density), followed by Ni–N<sub>3</sub>C<sub>1</sub> (−0.92 V) and Ni–N<sub>4</sub> (−1.03 V). Moreover, Liu *et al.*<sup>52</sup> applied a “slow-growth” sampling approach to evaluate the reaction barriers and showed that the Ni-atom coordinated with one N and three C atoms (Ni–N<sub>1</sub>C<sub>3</sub>) is most active and selective for the CO<sub>2</sub>RR. These indicate that the CO<sub>2</sub>RR activity tends to decrease with the increase of coordinated nitrogen, which is

qualitatively in good agreement with our DMol<sup>3</sup> results based on the simplified computational hydrogen electrode model.

In addition, since the HER usually competes with the CO<sub>2</sub>RR, it is thus also important to evaluate the selectivity between CO<sub>2</sub> reduction and HER by comparing their limiting potential ( $U_L$ ), which is defined as  $−\Delta G/e$  ( $\Delta G$  refers to the most sluggish step). According to this definition, a more positive  $\Delta U_L$  ( $U_L(\text{CO}_2) − U_L(\text{H}_2)$ ) means a higher selectivity toward the CO<sub>2</sub>RR (the limiting free energy change of the competitive HER,  $\Delta G_{\text{HER}}$ , is provided in Table S6†). From Fig. 5d, most of the Ni–B<sub>X</sub>C<sub>Y</sub>N<sub>Z</sub> catalysts are selective to the HER except for Ni–B<sub>0</sub>C<sub>3</sub>N<sub>1</sub>, Ni–B<sub>0</sub>C<sub>0</sub>N<sub>4</sub>, Ni–B<sub>1</sub>C<sub>0</sub>N<sub>3</sub>, Ni–B<sub>2</sub>C<sub>0</sub>N<sub>2-B-hex</sub>, Ni–B<sub>1</sub>C<sub>1</sub>N<sub>2-N-oppo</sub>, Ni–B<sub>1</sub>C<sub>1</sub>N<sub>2-N-hex</sub> and Ni–B<sub>2</sub>C<sub>1</sub>N<sub>1-B-pen</sub>. Among the 7 CO<sub>2</sub>RR selective catalysts, Ni–B<sub>0</sub>C<sub>3</sub>N<sub>1</sub> and Ni–B<sub>0</sub>C<sub>0</sub>N<sub>4</sub> are potentially determined by \*CO<sub>2</sub> hydrogenation. However, the  $\Delta G$  for \*COOH formation on Ni–B<sub>0</sub>C<sub>0</sub>N<sub>4</sub> is very high (1.49 eV), making Ni–B<sub>0</sub>C<sub>0</sub>N<sub>4</sub> selective but less active for the CO<sub>2</sub>RR. A recent report by Zhang *et al.*<sup>64</sup> showed that single Ni<sup>2+</sup> atoms fourfold coordinated by N and dispersed over a carbon black support displayed excellent CO Faraday efficiency (above 90%) and a low faradaic efficiency to H<sub>2</sub>. The higher CO selectivity of the Ni–N<sub>4</sub> catalyst over the HER is in agreement with our predictions of the CO<sub>2</sub>RR selective Ni–B<sub>0</sub>C<sub>0</sub>N<sub>4</sub>. Moreover, for the screened Ni–B<sub>1</sub>C<sub>0</sub>N<sub>3</sub>, Ni–B<sub>2</sub>C<sub>0</sub>N<sub>2-B-hex</sub>, Ni–B<sub>1</sub>C<sub>1</sub>N<sub>2-N-oppo</sub>, Ni–B<sub>1</sub>C<sub>1</sub>N<sub>2-N-hex</sub> and Ni–B<sub>2</sub>C<sub>1</sub>N<sub>1-B-pen</sub>, the \*CO desorption is the most sluggish step, and the corresponding  $\Delta G$  (\*CO) is −0.48 eV, −0.63 eV, −0.35 eV, −0.64 eV, and −1.25 eV, respectively. Since the CO<sub>2</sub>RR process requires rapid desorption of \*CO to improve the CO selectivity, Ni–B<sub>2</sub>C<sub>1</sub>N<sub>1-B-pen</sub> is thus excluded as a viable CO<sub>2</sub>RR catalyst due to its over strong \*CO adsorption. Note that CO<sub>2</sub> electroreduction can produce many possible products. Previous experimental studies have verified that the N/C coordinated Ni produces CO as the main product, hence we only focus on the CO pathway for the B-free Ni–B<sub>X</sub>C<sub>Y</sub>N<sub>Z</sub> ( $X = 0$ ). With regard to the B-coordinated systems, we select the 5 CO<sub>2</sub>RR selective catalysts (Ni–B<sub>1</sub>C<sub>0</sub>N<sub>3</sub>, Ni–B<sub>2</sub>C<sub>0</sub>N<sub>2-B-hex</sub>, Ni–B<sub>1</sub>C<sub>1</sub>N<sub>2-N-oppo</sub>, Ni–B<sub>1</sub>C<sub>1</sub>N<sub>2-N-hex</sub> and Ni–B<sub>2</sub>C<sub>1</sub>N<sub>1-B-pen</sub>) to further examine the possible HCOOH pathway. From Fig. S3,† the limiting potential required for HCOOH formation is much higher, which indicates that CO is the more preferred product. In addition, since the \*CO adsorption on Ni–B<sub>2</sub>C<sub>1</sub>N<sub>1-B-pen</sub> is very strong (−1.25 eV), we further studied its potential to produce more deep-reduced products. From Fig. S3e,† the \*CO can be further reduced to CH<sub>4</sub> and CH<sub>3</sub>OH, and the potential-determining step corresponds to hydrogenation of \*CHO to \*OCH<sub>2</sub> (0.92 eV).

### Activity origin

The activity of an electrocatalyst is known to be governed by its intrinsic electronic structure. To decode the underlying activity origin, we first analyzed the electronic structures, and the projected density of states (PDOS) of Ni and the coordination atoms (B, C and N) on pure Ni–B<sub>X</sub>C<sub>Y</sub>N<sub>Z</sub> catalysts is shown in Fig. S4.† Since all the investigated 25 catalysts are non-magnetic, there is no spin-polarization in the calculated electronic states; we thus only plotted one of the spin channels. In the C-

and N-coordinated Ni–B<sub>X</sub>C<sub>Y</sub>N<sub>Z</sub> (B-free,  $X = 0$ ), the electronic states around the Fermi level are mainly contributed by the Ni atom for Ni–B<sub>0</sub>C<sub>3</sub>N<sub>1</sub>, Ni–B<sub>0</sub>C<sub>2</sub>N<sub>2-N</sub>-oppo, Ni–B<sub>0</sub>C<sub>2</sub>N<sub>2-N</sub>-pen, and Ni–B<sub>0</sub>C<sub>2</sub>N<sub>2-N</sub>-hex (Fig. S4a, 2b, 2c and 2d†). While in the case of Ni–B<sub>0</sub>C<sub>1</sub>N<sub>3</sub> (Fig. S4e†) and Ni–B<sub>0</sub>C<sub>0</sub>N<sub>4</sub> (Fig. S4f†), the Ni electronic states shifted downward, and the Fermi levels are mainly contributed by the N atoms. This can qualitatively explain why Ni–B<sub>0</sub>C<sub>1</sub>N<sub>3</sub> and Ni–B<sub>0</sub>C<sub>0</sub>N<sub>4</sub> with higher N-content show lower CO<sub>2</sub>RR activity. We further analyzed the Bader charge of the Ni active center in Ni–B<sub>X</sub>C<sub>Y</sub>N<sub>Z</sub> (B-free,  $X = 0$ ) (Table S8†), where the Ni atom carries positive charge between +0.625|e| and +0.830|e|. Particularly, we note that the charge of the Ni atom in Ni–B<sub>0</sub>C<sub>3</sub>N<sub>1</sub> (+0.625|e|) is the lowest, indicating that the Ni atom has more electrons in the outer shell. The previous research studies reveal that the larger magnitude of electrons in the outer shell would facilitate the adsorption of CO<sub>2</sub> and \*COOH intermediates thereby accelerating the CO<sub>2</sub>RR.<sup>65,66</sup>

On the other hand, the electronic structures of B-coordinated Ni–B<sub>X</sub>C<sub>Y</sub>N<sub>Z</sub> ( $X \neq 0$ ) are much more complicated (Fig. S4g–2y†). Depending on the various coordination environments, the electronic states at the Fermi level are mainly contributed by the Ni atoms (Ni–B<sub>1</sub>C<sub>0</sub>N<sub>3</sub>, Ni–B<sub>2</sub>C<sub>0</sub>N<sub>2-B</sub>-pen, Ni–B<sub>2</sub>C<sub>0</sub>N<sub>2-B</sub>-hex, Ni–B<sub>1</sub>C<sub>2</sub>N<sub>1-C</sub>-oppo, Ni–B<sub>1</sub>C<sub>1</sub>N<sub>2-N</sub>-pen and Ni–B<sub>1</sub>C<sub>1</sub>N<sub>2-N</sub>-hex), the B atoms (Ni–B<sub>2</sub>C<sub>0</sub>N<sub>2-B</sub>-oppo, Ni–B<sub>2</sub>C<sub>2</sub>N<sub>0-C</sub>-hex and Ni–B<sub>2</sub>C<sub>1</sub>N<sub>1-B</sub>-pen), the Ni and B atoms (Ni–B<sub>3</sub>C<sub>0</sub>N<sub>1</sub>, Ni–B<sub>4</sub>C<sub>0</sub>N<sub>0</sub>, Ni–B<sub>3</sub>C<sub>1</sub>N<sub>0</sub>, Ni–B<sub>2</sub>C<sub>1</sub>N<sub>1-B</sub>-oppo, Ni–B<sub>2</sub>C<sub>1</sub>N<sub>1-B</sub>-hex and Ni–B<sub>1</sub>C<sub>1</sub>N<sub>2-N</sub>-oppo), or the Ni and C atoms (Ni–B<sub>2</sub>C<sub>2</sub>N<sub>0-C</sub>-oppo, Ni–B<sub>2</sub>C<sub>2</sub>N<sub>0-C</sub>-pen, Ni–B<sub>1</sub>C<sub>2</sub>N<sub>1-C</sub>-pen and Ni–B<sub>1</sub>C<sub>2</sub>N<sub>1-C</sub>-hex), respectively. In the B-coordinated systems, both the Ni and B atoms are positively charged (except for Ni–B<sub>4</sub>C<sub>0</sub>N<sub>0</sub> where the Ni atom has a negative charge of −0.0411|e|), and Ni is found to carry much less positive charge (+0.07–+0.49|e|) than B (+1.22–+1.51|e|). Compared to the B-free Ni–B<sub>X</sub>C<sub>Y</sub>N<sub>Z</sub> ( $X = 0$ ) (Ni atomic charge: +0.625–+0.830|e|),

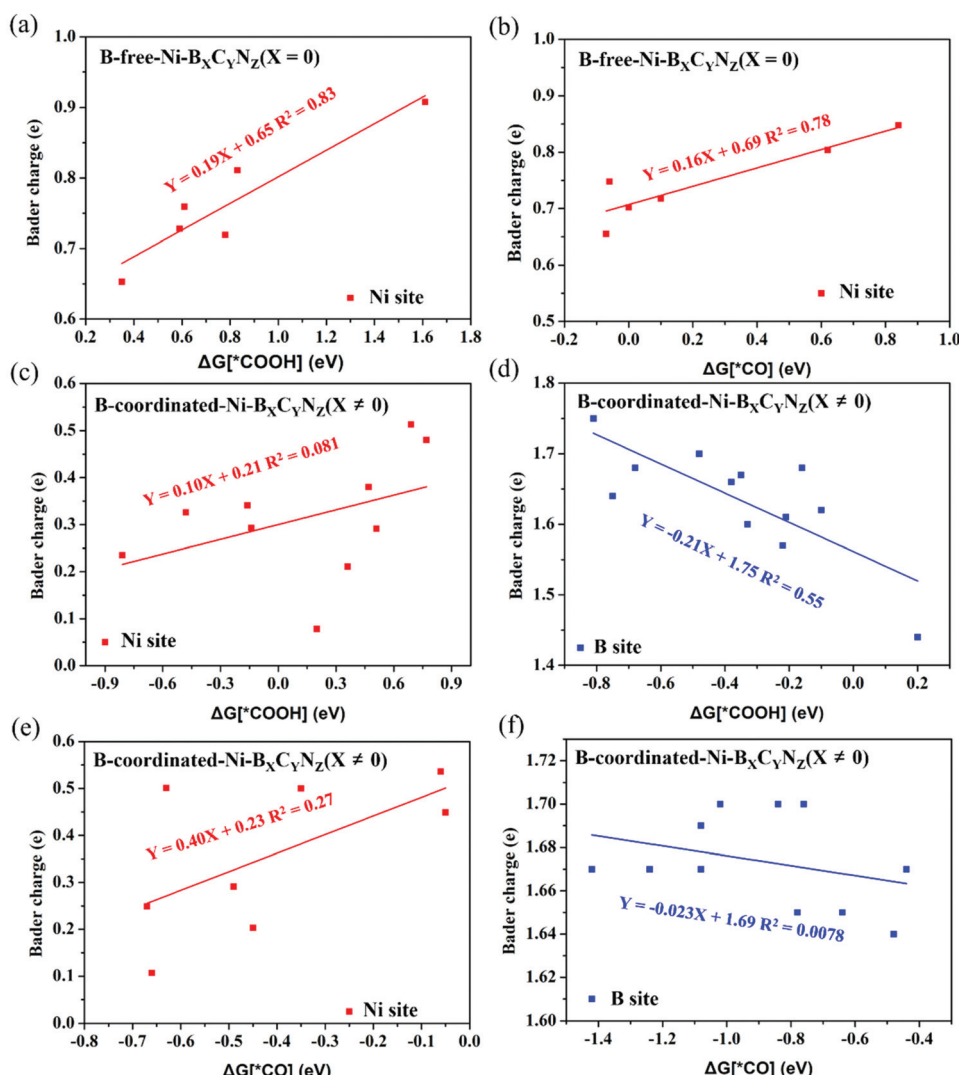


Fig. 6 Bader charge analysis of active sites (Ni or B atom) on \*COOH and \*CO adsorbed Ni–B<sub>X</sub>C<sub>Y</sub>N<sub>Z</sub>. Correlations of the adsorption free energy of \*COOH (a) and \*CO (b) intermediates with Ni Bader charge on B-free Ni–B<sub>X</sub>C<sub>Y</sub>N<sub>Z</sub> ( $X = 0$ ). Correlations of the adsorption free energy of \*COOH and \*CO intermediates with Ni (c, e) and B Bader charge (d, f) on B-coordinated Ni–B<sub>X</sub>C<sub>Y</sub>N<sub>Z</sub> ( $X \neq 0$ ).

the charge of the Ni atom is significantly reduced with the introduction of B (Table S8†). It is known that B behaves like a transition metal and can be the active site in electrocatalysis. The valence electronic configuration of B atoms is  $2s^22p^1$  and the  $sp^3$  hybridization of these orbitals can accept and donate the lone-pair electron, which is similar to the d orbital of transition metals.<sup>45,67,68</sup> In addition, the electronegativity of B (2.04) is close to that of Ni (1.91) and lower than C (2.55) and N (3.04), which also means that the B has transition-metal-like properties. This indicates that Ni and B can work synergistically to function as dual-active sites, which can explain the dual-site adsorption of  $\text{CO}_2$ , \*COOH and \*CO in some of the  $\text{Ni-B}_x\text{C}_y\text{N}_z$  ( $X \neq 0$ ) catalysts, leading to more favorable \*COOH formation and stronger \*CO adsorption.

Fig. 6 shows the correlation between the calculated Bader charge of the active center and the adsorption free energy of \*COOH and \*CO species. In the B-free  $\text{Ni-B}_x\text{C}_y\text{N}_z$  ( $X = 0$ ), only the Ni acts as the active site, and both the  $\Delta G$  (\*COOH) and  $\Delta G$  (\*CO) display linear correlation ( $R^2(*\text{COOH}) \approx 0.83$  and  $R^2(*\text{CO}) \approx 0.78$ ) with the Ni Bader charge (Fig. 6a and b). However, in the B-coordinated  $\text{B}_x\text{C}_y\text{N}_z$  ( $X \neq 0$ ), the active site varies with the coordination environment, and either the single Ni site, single B site or dual Ni-B site can be the catalytic active center. Due to the complexity in the bonding behaviors between  $\text{CO}_2\text{RR}$  intermediates and the active sites, the correlation between the atomic charge of Ni or B (Table S9†) with the adsorption free energy of \*COOH and \*CO is very poor (Fig. 6c–f). Compared to the single metal atom catalyst, the dual-site or multifunctional site catalysts need a more complex descriptor to explain the intrinsic activity, which would stimulate the future research on the dual- or multi-site electrocatalysts.

## Conclusion

In summary, based on DFT computations, we explored the coordination effect on the electrocatalytic activity of Ni SACs towards  $\text{CO}_2$  reduction, where the coordination atoms are C, N or B. Our results showed that the coordination environments of the metal atom have a remarkable influence on the adsorption and reaction characteristics. In the C and/or N coordinated  $\text{Ni-B}_x\text{C}_y\text{N}_z$  (B-free,  $X = 0$ ), only the Ni atom acts as the active site, which features as a single-site adsorption mode for  $\text{CO}_2\text{RR}$  intermediates. Differently, with the introduction of B ( $\text{Ni-B}_x\text{C}_y\text{N}_z$ ,  $X \neq 0$ ), the coordinated B atom and the Ni metal function as a dual-site and lead to versatile coordination modes of reaction species (single or dual-site adsorption) that varies with the type and number of coordination elements. The versatility in the adsorption modes also results in a weakened linear scaling relationship between \*COOH and \*CO. Moreover, we established the volcano-type activity plot. It is found that most of the B-coordinated  $\text{Ni-B}_x\text{C}_y\text{N}_z$  ( $X \neq 0$ ) catalysts are located in the left region where \*CO desorption becomes the most difficult step, while all the C and/or N coordinated  $\text{Ni-B}_x\text{C}_y\text{N}_z$  ( $X = 0$ ) are located in the right region where the \*COOH formation

becomes the potential-determining step. Our results predict that  $\text{Ni-B}_0\text{C}_3\text{N}_1$  and  $\text{Ni-B}_1\text{C}_1\text{N}_{2-\text{N-oppo}}$  stand out as the most active catalysts for the  $\text{CO}_2\text{RR}$  and have high selectivity over the HER. Hence, by precisely controlling the coordination environment, the experimentally available Ni SACs can be utilized as highly active and selective  $\text{CO}_2\text{RR}$  electrocatalysts. This work provides significant inspiration on boosting the electrocatalytic  $\text{CO}_2\text{RR}$  activity of Ni or other metal catalysts by regulating the coordination environment.

## Conflicts of interest

The authors declare no competing financial interests.

## Acknowledgements

This work was supported by the National Natural Science Foundation of China (No. 21903008), the Chongqing Science and Technology Commission (cstc2020jcyj-msxmX0382), and the Fundamental Research Funds for the Central Universities (2020CDJQY-A031, 2020CDJ-LHZZ-063). This research used resources of the National Supercomputer Center in Guangzhou.

## References

- 1 H. H. Chen, X. Guo, X. D. Kong, Y. L. Xing, Y. Liu, B. L. Yu, Q. X. Li, Z. G. Geng, R. Si and J. Zeng, *Green Chem.*, 2020, **22**, 7529–7536.
- 2 S. E. Schwartz, *Energy Environ. Sci.*, 2008, **1**, 430–453.
- 3 W. Choi, M. Kim, B. J. Kim, Y. Park, D. S. Han, M. R. Hoffmann and H. Park, *Appl. Catal., B*, 2020, **265**, 118607.
- 4 D. D. Zhu, J. L. Liu and S. Z. Qiao, *Adv. Mater.*, 2016, **28**, 3423–3452.
- 5 X. Zhang, Z. S. Wu, X. Zhang, L. W. Li, Y. Y. Li, H. M. Xu, X. X. Li, X. L. Yu, Z. S. Zhang, Y. Y. Liang and H. L. Wang, *Nat. Commun.*, 2017, **8**, 14675.
- 6 Q. Fan, P. F. Hou, C. H. Choi, T. S. Wu, S. Hong, F. Li, Y. L. Soo, P. Kang, Y. S. Jung and Z. Y. Sun, *Adv. Energy Mater.*, 2020, **10**, 1903068.
- 7 Y. W. Yue, Y. Y. Sun, C. Tang, B. Liu, Z. Ji, A. Q. Hu, B. Shen, Z. Z. Zhang and Z. Z. Sun, *Carbon*, 2019, **154**, 108–114.
- 8 S. Dou, J. J. Song, S. B. Xi, Y. H. Du, J. Wang, Z. F. Huang, Z. C. J. Xu and X. Wang, *Angew. Chem., Int. Ed.*, 2019, **58**, 4041–4045.
- 9 T. T. Zheng, K. Jiang and H. T. Wang, *Adv. Mater.*, 2018, **30**, 1802066.
- 10 H. Q. Zhou, X. L. Zou, X. Wu, X. Yang and J. Li, *J. Phys. Chem. Lett.*, 2019, **10**, 6551–6557.
- 11 X. L. Zhang, W. C. Wang and Z. X. Yang, *ACS Sustainable Chem. Eng.*, 2020, **8**, 6134–6141.

12 M. M. Zhao, H. Tang, Q. M. Yang, Y. L. Gu, H. Zhu, S. C. Yan and Z. G. Zou, *ACS Appl. Mater. Interfaces*, 2020, **12**, 4565–4571.

13 K. P. Kuhl, T. Hatsukade, E. R. Cave, D. N. Abram, J. Kibsgaard and T. F. Jaramillo, *J. Am. Chem. Soc.*, 2014, **136**, 14107–14113.

14 C. Kim, F. Dionigi, V. Beermann, X. L. Wang, T. Moller and P. Strasser, *Adv. Mater.*, 2019, **31**, 1805617.

15 R. Shi, J. H. Guo, X. R. Zhang, G. I. N. Waterhouse, Z. J. Han, Y. X. Zhao, L. Shang, C. Zhou, L. Jiang and T. R. Zhang, *Nat. Commun.*, 2020, **11**, 3028.

16 Y. R. Wang, R. X. Yang, Y. F. Chen, G. K. Gao, Y. J. Wang, S. L. Li and Y. Q. Lan, *Sci. Bull.*, 2020, **65**, 1635–1642.

17 F. P. Pan, B. Y. Li, E. Sarnello, S. Hwang, Y. Gang, X. H. Feng, X. M. Xiang, N. M. Adli, T. Li, D. Su, G. Wu, G. F. Wang and Y. Li, *Nano Energy*, 2020, **68**, 104384.

18 R. Sui, J. J. Pei, J. J. Fang, X. J. Zhang, Y. F. Zhang, F. J. Wei, W. X. Chen, Z. Hu, S. Hu, W. Zhu and Z. B. Zhuang, *ACS Appl. Mater. Interfaces*, 2021, **13**, 17736–17744.

19 T. N. Nguyen, M. Salehi, Q. V. Le, A. Seifitokaldani and C. T. Dinh, *ACS Catal.*, 2020, **10**, 10068–10095.

20 F. P. Pan, B. Y. Li, E. Sarnello, Y. H. Fei, X. H. Feng, Y. Gang, X. M. Xiang, L. Z. Fang, T. Li, Y. H. Hu, G. F. Wang and Y. Li, *ACS Catal.*, 2020, **10**, 10803–10811.

21 Y. Pan, R. Lin, Y. Chen, S. Liu, W. Zhu, X. Cao, W. Chen, K. Wu, W.-C. Cheong, Y. Wang, L. Zheng, J. Luo, Y. Lin, Y. Liu, C. Liu, J. Li, Q. Lu, X. Chen, D. Wang, Q. Peng, C. Chen and Y. Li, *J. Am. Chem. Soc.*, 2018, **140**, 4218–4221.

22 X. G. Li, W. T. Bi, M. L. Chen, Y. X. Sun, H. X. Ju, W. S. Yan, J. F. Zhu, X. J. Wu, W. S. Chu, C. Z. Wu and Y. Xie, *J. Am. Chem. Soc.*, 2017, **139**, 14889–14892.

23 Y. Hou, Y.-L. Liang, P.-C. Shi, Y.-B. Huang and R. Cao, *Appl. Catal., B*, 2020, **271**, 118929.

24 H. N. Zhang, J. Li, S. B. Xi, Y. H. Du, X. Hai, J. Y. Wang, H. M. Xu, G. Wu, J. Zhang, J. Lu and J. Z. Wang, *Angew. Chem., Int. Ed.*, 2019, **58**, 14871–14876.

25 C. Zhang, Z. Fu, Q. Zhao, Z. Du, R. Zhang and S. Li, *Electrochim. Commun.*, 2020, **116**, 106758.

26 W. Ju, A. Bagger, G. P. Hao, A. S. Varela, I. Sinev, V. Bon, B. Roldan Cuenya, S. Kaskel, J. Rossmeisl and P. Strasser, *Nat. Commun.*, 2017, **8**, 944.

27 J. K. Li, P. Prslja, T. Shinagawa, A. J. M. Fernandez, F. Krumeich, K. Artyushkova, P. Atanassov, A. Zitolo, Y. C. Zhou, R. Garcia-Muelas, N. Lopez, J. Perez-Ramirez and F. Jaouen, *ACS Catal.*, 2019, **9**, 10426–10439.

28 T. Asset, S. T. Garcia, S. Herrera, N. Andersen, Y. C. Chen, E. J. Peterson, I. Matanovic, K. Artyushkova, J. Lee, S. D. Minteer, S. Dai, X. Q. Pan, K. Chavan, S. C. Barton and P. Atanassov, *ACS Catal.*, 2019, **9**, 7668–7678.

29 W. Z. Zheng, J. Yang, H. Q. Chen, Y. Hou, Q. Wang, M. Gu, F. He, Y. Xia, Z. Xia, Z. J. Li, B. Yang, L. C. Lei, C. Yuan, Q. G. He, M. Qiu and X. L. Feng, *Adv. Funct. Mater.*, 2020, **30**, 1907658.

30 C. Xu, X. Zhi, V. Anthony, D. Wang, B. Jin, Y. Jiao, Y. Zheng and S.-Z. Qiao, *Small Struct.*, 2020, **2**, 2000058.

31 F. P. Pan, W. Deng, C. Justiniano and Y. Li, *Appl. Catal., B*, 2018, **226**, 463–472.

32 X. M. Hu, H. H. Hval, E. T. Bjerglund, K. J. Dalgaard, M. R. Madsen, M. M. Pohl, E. Welter, P. Lamagni, K. B. Buhl, M. Bremholm, M. Beller, S. U. Pedersen, T. Skrydstrup and K. Daasbjerg, *ACS Catal.*, 2018, **8**, 6255–6264.

33 T. Moller, W. Ju, A. Bagger, X. L. Wang, F. Luo, T. N. Thanh, A. S. Varela, J. Rossmeisl and P. Strasser, *Energy Environ. Sci.*, 2019, **12**, 640–647.

34 W. Zheng, F. Chen, Q. Zeng, Z. Li, B. Yang, L. Lei, Q. Zhang, F. He, X.-L. Wu and Y. Hou, *Nanomicro Lett.*, 2020, **12**, 108.

35 C. M. Zhao, X. Y. Dai, T. Yao, W. X. Chen, X. Q. Wang, J. Wang, J. Yang, S. Q. Wei, Y. E. Wu and Y. D. Li, *J. Am. Chem. Soc.*, 2017, **139**, 8078–8081.

36 K. Jiang, S. Siahrostami, A. J. Akey, Y. B. Li, Z. Y. Lu, J. Lattimer, Y. F. Hu, C. Stokes, M. Gangishetty, G. X. Chen, Y. W. Zhou, W. Hill, W. B. Cai, D. Bell, K. R. Chan, J. K. Norskov, Y. Cui and H. T. Wang, *Chem.*, 2017, **3**, 950–960.

37 H. B. Yang, S. F. Hung, S. Liu, K. D. Yuan, S. Miao, L. P. Zhang, X. Huang, H. Y. Wang, W. Z. Cai, R. Chen, J. J. Gao, X. F. Yang, W. Chen, Y. Q. Huang, H. M. Chen, C. M. Li, T. Zhang and B. Liu, *Nat. Energy*, 2018, **3**, 140–147.

38 P. F. Yao, J. W. Zhang, Y. L. Qiu, Q. Zheng, H. M. Zhang, J. W. Yan and X. F. Li, *ACS Sustainable Chem. Eng.*, 2021, **9**, 5437–5444.

39 C. C. Yan, H. B. Li, Y. F. Ye, H. H. Wu, F. Cai, R. Si, J. P. Xiao, S. Miao, S. H. Xie, F. Yang, Y. S. Li, G. X. Wang and X. H. Bao, *Energy Environ. Sci.*, 2018, **11**, 1204–1210.

40 Y. J. Sa, H. Jung, D. Shin, H. Y. Jeong, S. Ringe, H. Kim, Y. J. Hwang and S. H. Joo, *ACS Catal.*, 2020, **10**, 10920–10931.

41 X. Rong, H. J. Wang, X. L. Lu, R. Si and T. B. Lu, *Angew. Chem., Int. Ed.*, 2020, **59**, 1961–1965.

42 Y. N. Gong, L. Jiao, Y. Y. Qian, C. Y. Pan, L. R. Zheng, X. C. Cai, B. Liu, S. H. Yu and H. L. Jiang, *Angew. Chem., Int. Ed.*, 2020, **59**, 2705–2709.

43 X. Yang, J. Cheng, X. Yang, Y. Xu, W. F. Sun, N. Liu and J. Z. Liu, *ACS Sustainable Chem. Eng.*, 2021, **9**, 6438–6445.

44 Y. Xia, X. Zhao, C. Xia, Z.-Y. Wu, P. Zhu, J. Y. T. Kim, X. Bai, G. Gao, Y. Hu, J. Zhong, Y. Liu and H. Wang, *Nat. Commun.*, 2021, **12**, 4225.

45 C. Y. Ling, X. H. Niu, Q. Li, A. J. Du and J. L. Wang, *J. Am. Chem. Soc.*, 2018, **140**, 14161–14168.

46 M. M. He, W. An, Y. Q. Wang, Y. Men and S. Liu, *Small*, 2021, **8**, 2104445.

47 X. Luo, J. Yang, H. Liu, X. Wu, Y. Wang, Y. Ma, S.-H. Wei, X. Gong and H. Xiang, *J. Am. Chem. Soc.*, 2011, **133**, 16285–16290.

48 X. Li, X. Yong, M. Wu, S. Lu, H. Liu, S. Meng, J. S. Tse and Y. Li, *J. Phys. Chem. Lett.*, 2019, **10**, 2554–2560.

49 A. Abengózar, D. Sucunza, P. García-García, D. Sampedro, A. Pérez-Redondo and J. J. Vaquero, *J. Org. Chem.*, 2019, **84**, 7113–7122.

50 S. Carenco, D. Portehault, C. Boissiere, N. Mezailles and C. Sanchez, *Chem. Rev.*, 2013, **113**, 7981–8065.

51 M. D. Hossain, Y. F. Huang, T. H. Yu, W. A. Goddard and Z. T. Luo, *Nat. Commun.*, 2020, **11**, 2256.

52 X. H. Zhao and Y. Y. Liu, *J. Am. Chem. Soc.*, 2020, **142**, 5773–5777.

53 B. Delley, *J. Chem. Phys.*, 2000, **113**, 7756–7764.

54 J. P. Perdew, K. Burke and M. Ernzerhof, *Phys. Rev. Lett.*, 1996, **77**, 3865–3868.

55 M. Ernzerhof and G. E. Scuseria, *J. Chem. Phys.*, 1999, **110**, 5029–5036.

56 B. Delley, *Phys. Rev. B: Condens. Matter Mater. Phys.*, 2002, **66**, 155125.

57 A. Klamt, *J. Phys. Chem.*, 1995, **99**, 2224–2235.

58 H. J. Monkhorst and J. D. Pack, *Phys. Rev. B: Solid State*, 1976, **13**, 5188–5192.

59 Q. Tang, Y. J. Lee, D. Y. Li, W. Choi, C. W. Liu, D. Lee and D. E. Jiang, *J. Am. Chem. Soc.*, 2017, **139**, 9728–9736.

60 Z. A. Piazza, H. S. Hu, W. L. Li, Y. F. Zhao, J. Li and L. S. Wang, *Nat. Commun.*, 2014, **5**, 3113.

61 S. Wang, L. Li, J. Li, C. Z. Yuan, Y. Kang, K. S. Hui, J. T. Zhang, F. Bin, X. Fan, F. M. Chen and K. N. Hui, *J. Phys. Chem. C*, 2021, **125**, 7155–7165.

62 F. H. Li and Q. Tang, *J. Mater. Chem. A*, 2021, **9**, 8761–8771.

63 H. A. Hansen, J. B. Varley, A. A. Peterson and J. K. Norskov, *J. Phys. Chem. Lett.*, 2013, **4**, 388–392.

64 H. Z. Yang, L. Shang, Q. H. Zhang, R. Shi, G. I. N. Waterhouse, L. Gu and T. R. Zhang, *Nat. Commun.*, 2019, **10**, 4585.

65 S. Fang, X. R. Zhu, X. K. Liu, J. Gu, W. Liu, D. H. Wang, W. Zhang, Y. Lin, J. L. Lu, S. Q. Wei, Y. F. Li and T. Yao, *Nat. Commun.*, 2020, **11**, 14848.

66 M. H. Sun, J. P. Ji, M. Y. Hu, M. Y. Weng, Y. P. Zhang, H. S. Yu, J. J. Tang, J. C. Zheng, Z. Jiang, F. Pan, C. D. Liang and Z. Lin, *ACS Catal.*, 2019, **9**, 8213–8223.

67 F. H. Li and Q. Tang, *Nanoscale*, 2019, **11**, 18769–18778.

68 M. A. Legare, G. Belanger-Chabot, R. D. Dewhurst, E. Welz, I. Krummenacher, B. Engels and H. Braunschweig, *Science*, 2018, **359**, 896–899.